Pointwise and mean-square conditions for residual correction of state estimators: a trust-region UKF–ANFIS framework for cascaded SOC and SOH estimation in VRLA gel batteries

Otabek Boltaev[1], Igor Kolesnikov[2], Karimberdi Karshiev[3]
Department of Electrical Engineering, Tashkent State Transport University,
1 Temiryulchilar Street, 100167 Tashkent, Uzbekistan
[3]Corresponding author
E-mail: [1]*boltayev_o@tstu.uz*, [2]*kolesnikovigor1944@gmail.com*, [3]*karimberdiqarshiyev@gmail.com*

Received 3 August 2026; accepted 6 September 2026; published online 23 November 2026
DOI https://doi.org/10.21595/mme.2026.26925

Check for updates

Copyright © 2026 Otabek Boltaev, et al. This is an open access article distributed under the Creative Commons Attribution License, which permits unrestricted use, distribution, and reproduction in any medium, provided the original work is properly cited.

Abstract. Accurate state-of-charge (SOC) and state-of-health (SOH) estimation is essential for stationary valve-regulated lead-acid (VRLA) gel batteries. Residual-correction hybrids are widely used, but a non-zero learned correction can increase rather than reduce a Kalman-filter error. We derive a necessary and sufficient pointwise condition for non-degradation, the mean-square condition for a shrinkage-scaled correction, and a closed-form expression for the optimal attainable reduction in terms of the uncentred alignment coefficient between the learned correction and the baseline error. Because the true error is unavailable online, the theorem is not itself an implementable guarantee. We therefore introduce covariance-based trust-region projection and an innovation gate as observable risk controls and prove a conditional mean-square boundedness result. The construction is instantiated by an ANFIS residual model applied to a parameter-augmented UKF. Corrected SOC, together with four explicitly defined health indices, feeds a second ANFIS stage for SOH. Evaluation uses a structurally distinct 2RC-hysteresis data generator, a 24-month ageing horizon, disjoint train/validation/test profiles, and paired repeated-Monte-Carlo analysis. Across eleven estimators (the proposed method plus ten baselines, including a protocol-matched implementation of the published EKF-ANN architecture of Dao et al.), the proposed SOC estimator obtained the lowest RMSE, 0.942 %, versus 1.314 % for its UKF baseline and 1.022 % for the linear-correction ablation. The test-set alignment coefficient was 0.716, corresponding to an optimal attainable RMSE reduction of 30.2 %; the validation-scaled correction achieved 28.3 %. Under a sign-reversed stress test, strict projection and gating reduced the damage relative to an ungated correction but did not preserve baseline RMSE, confirming that the online controls are risk-limiting surrogates rather than a pointwise guarantee. The SOH ANFIS stage was outperformed by a linear corrector, which is reported as a limitation.

Keywords: state of charge, state of health, lead-acid battery, unscented Kalman filter, residual correction, non-degradation condition, trust-region projection, neuro-fuzzy inference, repeated Monte Carlo validation.

1. Introduction

1.1. Background and motivation

Stationary VRLA batteries support safety-critical backup loads in transport, telecommunications, utility protection and industrial control. Railway signalling and relay-protection systems are one intended application, but the present study does not use field telemetry and is therefore evaluated as a general stationary-VRLA estimation study. Global battery demand for electric transport and stationary storage exceeded 1 TWh in 2024 [1]. SOC describes presently available charge, whereas SOH represents the cumulative and largely

irreversible loss of capacity and growth of internal resistance relative to beginning of life [2]. The signalling circuits these banks protect [3] and the traction power supply that surrounds them [4] are themselves subjects of active modelling work. A further motivation is material rather than operational: lead–acid cells are a dominant source of lead-bearing industrial waste [5], so any diagnostic method that defers premature replacement carries a lifecycle benefit beyond reliability.

1.2. State of the art

Coulomb counting and static open-circuit-voltage (OCV) look-up tables accumulate integration drift and cannot account for capacity fade [6]. Model-based recursive estimators mitigate this by combining an equivalent circuit model (ECM) with a state observer. He, Xiong and Fan compared ECM topologies for SOC estimation accuracy [7]; Simić et al. and Estaller et al. addressed embedded-hardware Randles-circuit identification and impedance modelling [8], [9]. Plett formalised the Extended Kalman Filter (EKF) for joint state and parameter estimation in battery management systems [10], building on Kalman's linear filtering theory [11]. For strongly nonlinear operating regions – including the shallow-slope regions of the OCV–SOC curve typical of lead-acid chemistries – the Unscented Kalman Filter (UKF) propagates a deterministic sigma-point set through the exact nonlinear model rather than relying on a first-order Jacobian [12], and comparative studies confirm its advantage at modest additional computational cost [13], [14].

In parallel, data-driven techniques have been applied to battery diagnostics. Jang's adaptive neuro-fuzzy inference system (ANFIS) combines fuzzy-rule interpretability with neural-network learning [15] and was applied to SOC estimation by Cai, Du and Liu [16]. Because ANFIS requires no explicit electrochemical model it can capture nonlinearities that are difficult to parameterise analytically, but its predictions are not constrained by the underlying physics and its extrapolation behaviour is difficult to guarantee. This has motivated hybrid physics/data-driven estimators; Cui et al. reviewed neural-network-Kalman-filter combinations and reported improved robustness relative to either constituent alone [17]. SOH estimation has followed an analogous trajectory, from mechanistic ageing studies of lead-acid systems [18-21] and lifetime models for irregular duty [22] to critical reviews of monitoring and data-driven diagnosis [2], [23], [24], [25]. The same shift from threshold-based inspection to learned condition indicators is visible across transport-asset diagnostics more broadly; a risk-oriented predictive-diagnostics framework built on learned vibration features is reported in [26], and shares with the present work the problem of validating a data-driven indicator against a physically meaningful reference.

1.3. The unresolved mathematical gap

Residual-correction architectures use a learned model to predict and cancel the error of a designated physics-based estimator. A zero correction reproduces the baseline, but this fact does not protect against a non-zero correction of the wrong sign or excessive magnitude. The mathematical question is therefore not whether the hybrid contains the baseline as a special case, but which conditions make a correction beneficial and how much improvement is attainable. Section 3.4 answers these questions for an additive scalar correction independently of the learner and the baseline filter, while distinguishing the exact oracle condition from the observable risk controls used online.

These three questions are answerable and are the subject of this paper. They are answerable, moreover, in a form that is independent of the particular learner and of the particular baseline filter: the results of Section 3.4 hold for any additive correction of any unbiased or biased scalar state estimate, with ANFIS and the UKF serving as an instantiation rather than as a restriction.

1.4. Contributions

The specific contributions of this paper are:

(1) A necessary and sufficient pointwise condition (Proposition 1) for an additive residual correction to reduce the absolute estimation error of an arbitrary baseline estimator, together with the corresponding mean-square condition for a shrinkage-scaled correction (Proposition 2).

(2) A closed-form expression for the optimal attainable mean-square error, $MSE_{hyb} = (1 - \rho_0^2)MSE_{base}$, where ρ_0 is the uncentred alignment coefficient between the raw learned correction and the baseline error (Corollary 1).

(3) A covariance-based trust-region projection and an innovation gate that use only online filter quantities, together with a conditional boundedness result and an adversarial stress test that explicitly measures – rather than assumes – their risk-limiting effect.

(4) A direct empirical test of Corollary 1 under structural model mismatch and strictly disjoint profiles: $\rho_0 = 0.716$ on the independent test conditions implies an optimal attainable RMSE reduction of 30.2 %, while validation-set scaling achieved 28.3 %.

(5) A comparison with ten baselines, including proportional and linear correction ablations and a protocol-matched published EKF–ANN architecture, together with an explicit negative result for the over-parameterised SOH ANFIS stage.

2. Cell modelling, degradation mechanisms and ageing dynamics

2.1. Degradation mechanisms in VRLA gel cells

In VRLA gel cells the dominant end-of-life mechanisms are anodic corrosion of the positive grid, degradation and shedding of the positive active mass, irreversible recrystallisation of lead sulfate in the active mass, and loss of water through gassing; these mechanisms are interdependent, since grid corrosion raises the resistance to current flow, which in turn impedes proper charging of parts of the active mass and promotes sulfation [18]. The term “sulfation” is frequently applied loosely, and its correct usage refers specifically to the growth of coarse, poorly soluble $PbSO_4$ crystals that are no longer readily reconverted on charge [19]. Failure-mode studies specific to valve-regulated designs identify additional VRLA-specific pathways associated with the immobilised electrolyte and the oxygen-recombination cycle [20], and operation under high-rate partial-state-of-charge duty – characteristic of standby banks subjected to repeated shallow discharge – has been shown to produce a distinct negative-plate failure mode [21].

All of these mechanisms reduce the effective active-material area and increase the ohmic and charge-transfer resistance, manifesting macroscopically as a simultaneous decline in usable capacity and a rise in internal resistance. Because they evolve slowly relative to the charge/discharge timescale, they are not observable from instantaneous current and voltage measurements and must be inferred from their cumulative influence on resistance- and capacity-related indices tracked over time – a constraint that directly motivates the two-timescale evaluation horizon adopted in Section 4.1.

2.2. Temperature dependence of internal resistance

Ionic mobility within the immobilised silica-gel electrolyte decreases at low temperature, increasing ohmic resistance, while elevated temperature accelerates both charge-transfer kinetics and the undesirable corrosion and water-loss processes above. This dependence is modelled through an Arrhenius-type correction of the nominal internal resistance:

$$R_0(T, SOH) = R_{0,nom}\left[1 + \alpha\left(T - T_{ref}\right) + \beta(1 - SOH)\right], \tag{1}$$

where $R_{0,nom}$ is the nominal resistance at the reference temperature T_{ref} = 20 °C, α is a

temperature-sensitivity coefficient and β a degradation-sensitivity coefficient that amplifies the resistance increase as SOH declines. This coupling motivates the resistance-based health index defined in Section 3.5.

2.3. Equivalent circuit topology

The estimator represents the cell terminal voltage by a first-order Thévenin (1RC) equivalent circuit:

$$V_t = OCV(SOC, T) - I\,R_0(T, SOH) - V_p, \tag{2}$$

$$\frac{dV_p}{dt} = -\frac{V_p}{R_1 C_1} + \frac{I}{C_1}, \tag{3}$$

with SOC dynamics expressed through Coulomb counting:

$$SOC(t) = SOC_0 - \frac{1}{Q(t)} \int_0^t i\,(\tau)\,d\tau, \tag{4}$$

where $Q(t)$ is the instantaneous usable capacity. It is essential to the validity of the evaluation reported in Section 5 that the data-generating model is NOT of this form; the generator is specified separately in Section 4.1.

2.4. Long-horizon ageing dynamics

Capacity fade and resistance growth are represented by a transparent empirical scenario model inspired by the stress-factor structure of Schiffer et al. [22]. It is not claimed as a chemistry-identification model fitted to this cell. For monthly session index m, the implemented recursions are:

$$q_m = \frac{Q_m}{Q_0} = 1 - k_{cyc} A_m^w - k_{cal}\sqrt{m}, \tag{5}$$

$$r_m = \frac{R_{0,nom,m}}{R_{0,0}} = 1 + \gamma_{corr} C_m, \tag{6}$$

$$SOH_m = w_Q q_m + w_R(2 - r_m), \qquad w_Q + w_R = 1, \tag{7}$$

where w_j is a stress weighting that penalises throughput accumulated at low SOC and at elevated temperature, and γ_{corr} and E_a govern Arrhenius-driven grid corrosion. Under this formulation SOH is monotonically non-increasing by construction, which is the physically required behaviour for a cumulative, largely irreversible degradation quantity and which the previous reference trajectory did not exhibit.

The accumulated stress terms are $A_m^w = \sum_{l<m} |\Delta Ah_l| \left[1 + 1.9\left(1 - \overline{SOC_l}\right)\right] \exp\left[0.045\left(\overline{T_l} - T_{ref}\right)\right]$ and $C_m = \sum_{\ell<m} \exp\left[c_T\left(\overline{T_l} - T_{ref}\right)\right]$. Table 1 reports every numerical parameter and distinguishes manufacturer values from scenario-calibrated coefficients. The resulting reference SOH is monotone by construction.

2.5. Boundary conditions and standards

The framework was parameterised for a single 2 V Sonnenschein A602/280 (5 OPzV 250) VRLA gel cell. The rated capacity of 280 A·h and nominal internal resistance of 0.79 mΩ at 20 °C were taken from the manufacturer data sheet [27]. The battery qualification context follows IEC 60896-21 [28]. Railway signaling is retained only as a motivating use case; neither the title nor

the validation claims describe the simulated duty as field-validated railway operation.

Table 1. Ageing-model parameters used in simulation. Parameters labelled scenario calibration were selected before test evaluation and are not manufacturer-identified degradation constants

Parameter	Value	Unit	Source / role
Q_0	280	A·h	Manufacturer data sheet [27]
$R_{0,0}$	0.79	mΩ at 20 °C	Manufacturer data sheet [27]
k_{cyc}	2.4×10^{-5}	(weighted A·h)$^{-1}$	Scenario calibration; not identified from test data
k_{cal}	0.0100	month$^{-1/2}$	Scenario calibration; not identified from test data
γ_{corr}	5.6×10^{-3}	month^{-1}	Scenario calibration; not identified from test data
c_T	0.050	K^{-1}	Effective corrosion-temperature scaling in the code
w_Q, w_R	0.70, 0.30	–	Fixed capacity/resistance weighting
Low-SOC factor	1.9	–	Fixed stress scaling in the code
Throughput T factor	0.045	K^{-1}	Fixed stress scaling in the code

3. Proposed framework

3.1. Cascaded architecture

The data-driven component acts as a residual-correction module applied to a single, empirically selected baseline filter, rather than as an independently trained full-state predictor fused with the filter. The architecture is cascaded: a parameter-augmented UKF stage produces the corrected SOC estimate, which is then propagated, together with four health indices, to a neuro-fuzzy SOH stage. We deliberately avoid the term "joint estimation", which properly denotes simultaneous recursive update of SOC- and SOH-related states within a single coupled state-space formulation; that is not what the present architecture does.

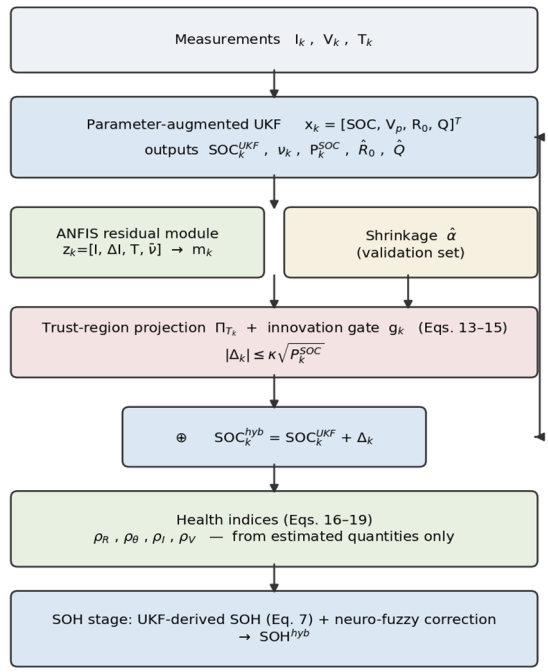

Fig. 1. Cascaded two-stage estimation architecture with trust-region enforcement

The complete structure, including the augmented state vector, the trust-region projection block and the innovation feedback path into the correction module, is shown in Fig. 1.

3.2. Augmented state-space formulation and baseline filters

The augmented state vector is:

$$\mathbf{x}_k = \left[SOC_k,\ V_{p,k},\ R_{0,k},\ Q_k\right]^T, \tag{8}$$

evolving according to the nonlinear discrete-time model:

$$\mathbf{x}_k = f(\mathbf{x}_{k-1}, u_{k-1}) + \mathbf{w}_{k-1}, \qquad y_k = h(\mathbf{x}_k, u_k) + v_k, \tag{9}$$

where u_k is the measured branch current, y_k the measured terminal voltage, and w_k, v_k the process and measurement noise. The parameters R_0 and Q are modelled as random-walk states with process-noise variances chosen to reflect their respective timescales – slow for capacity, faster for resistance – so that no true parameter value generated by the simulator is ever supplied to any estimator. All health indices of Section 3.5 are computed exclusively from the estimated values $\hat{R}_0$ and $\hat{Q}$. R_1 is not estimated online and does not enter any index; the polarisation branch is represented by the state V_p, whose contribution to the terminal voltage is already accounted for in the measurement model.

The EKF linearises f and h about the current estimate through the Jacobians $F_k = \frac{\partial f}{\partial x}$ and $H_k = \frac{\partial h}{\partial x}$ and propagates state and covariance through the standard predict-update recursion [10], [29]:

$$\hat{\mathbf{x}}_{k|k-1} = f\left(\hat{\mathbf{x}}_{k-1|k-1}, u_{k-1}\right), \qquad \mathbf{P}_{k|k-1} = \mathbf{F}_k \mathbf{P}_{k-1|k-1} \mathbf{F}_k^T + \mathbf{Q}_w, \tag{10}$$

$$\mathbf{K}_k = \mathbf{P}_{k|k-1} \mathbf{H}_k^T \left(\mathbf{H}_k \mathbf{P}_{k|k-1} \mathbf{H}_k^T + R_v\right)^{-1}, \qquad \hat{\mathbf{x}}_{k|k} = \hat{\mathbf{x}}_{k|k-1} + \mathbf{K}_k \nu_k. \tag{11}$$

For both EKF and UKF, the SOH proxy is obtained by substituting the corresponding online estimates $\hat{R}_0$, k and $\hat{Q}_k$ into Eq. (7). The implemented SOH cascade uses the UKF parameter estimates; the former label "EKF-based SOH" has therefore been corrected throughout.

3.3. Residual-correction module: specification

A Sugeno-type ANFIS module [15], following the battery-diagnostics application pattern of Cai et al. [16], is trained to predict the residual error of the UKF SOC estimate. Its input vector is:

$$\mathbf{z}_k = [I_k, \Delta I_k, T_k, \bar{\nu}_k]^T, \qquad \bar{\nu}_k = \frac{\nu_k}{\sqrt{\mathbf{H}_k \mathbf{P}_{k|k-1} \mathbf{H}_k^T + R_v}}, \tag{12}$$

that is, current, current rate of change, cell temperature and the normalised innovation. The module configuration is as shown in Table 2.

The standalone ANFIS baseline is given matched model capacity, sample count, epoch budget and normalisation. It differs only in its inputs and target, as summarised in Table 3; this prevents an implementation-capacity advantage from being attributed to the residual-learning strategy.

Table 2. Configuration of the ANFIS residual-correction module

Item	Setting
Inputs	4: I, ΔI, T, normalised innovation $\bar{\nu}$
Membership functions	2 generalised bell functions per input → 16 rules
Consequents	First-order Sugeno, linear in the four inputs
Initialisation	Grid partition; centres at training 10th/90th percentiles
Input normalisation	z-score; training-set mean and s.d. frozen thereafter
Training algorithm	Hybrid regularised least squares / gradient descent
Epochs	60 maximum; 25 used after early stopping
Stopping criterion	Validation RMSE; patience 8 epochs
Training samples	12 000 sampled observations from 18 complete runs
Validation samples	6 000 sampled observations from 6 complete runs
Initialisation seed	7
Retraining policy	Trained once and frozen for all 24 test runs

Table 3. Matched configuration of the residual corrector and standalone ANFIS baseline

Item	Residual corrector	Standalone predictor
Target	UKF residual e_k	SOC directly
Inputs	I, ΔI, T, $\bar{\nu}$ (filter innovation)	I, ΔI, T, V (no filter output available)
Membership functions	2 gbellmf per input	2 gbellmf per input
Rules	16	16
Consequents	first-order Sugeno	first-order Sugeno
Training algorithm	hybrid LSE / gradient descent	hybrid LSE / gradient descent
Epoch budget / stopping	60 max, early stopping, patience 8	60 max, early stopping, patience 8
Training samples	12 000	12 000
Normalisation	z-score, training-set statistics frozen	z-score, training-set statistics frozen

3.4. Non-degradation condition and trust-region enforcement

Let $e_k = SOC_k^{true} - \hat{SOC}_k^{UKF}$ denote the baseline error and let the corrected estimate be $\hat{SOC}_k^{hyb} = \hat{SOC}_k^{UKF} + \Delta_k$, so that the corrected error is $\tilde{e}_k = e_k - \Delta_k$.

Proposition 1 (pointwise non-degradation). For every k, $|\tilde{e}_k| \le |e_k|$ if and only if $\Delta_k(\Delta_k - 2e_k) \le 0$, equivalently if and only if $\operatorname{sgn}(\Delta_k) = \operatorname{sgn}(e_k)$ and $|\Delta_k| \le 2|e_k|$. The inequality is strict if and only if $0 < \Delta_k \operatorname{sgn}(e_k) < 2|e_k|$:

$$|\tilde{e}_k| \le |e_k| \Leftrightarrow \Delta_k(\Delta_k - 2e_k) \le 0 \Leftrightarrow \operatorname{sgn}(\Delta_k) = \operatorname{sgn}(e_k),\ |\Delta_k| \le 2|e_k|. \tag{13}$$

Proof. $\tilde{e}_k^2 - e_k^2 = (e_k - \Delta_k)^2 - e_k^2 = \Delta_k^2 - 2\Delta_k e_k = \Delta_k(\Delta_k - 2e_k)$. The product is non-positive precisely when Δ_k lies between 0 and $2e_k$ inclusive, which for $e_k \neq 0$ is the stated sign-and-magnitude condition. □

Proposition 1 makes the risk explicit: a correction of the wrong sign degrades the estimate for any magnitude whatsoever, and a correction of the correct sign degrades it as soon as it overshoots by more than a factor of two. Neither failure is excluded by the fact that a zero correction is harmless.

Proposition 2 (mean-square condition under shrinkage). Let m_k be the raw output of the learned model and let $\Delta_k = \alpha m_k$ for a scalar shrinkage gain α. Write $J(\alpha) = E[\tilde{e}^2]$. Then $J(\alpha) = E[e^2] - 2\alpha E[me] + \alpha^2 E[m^2]$, which is strictly convex in α whenever $E[m^2] > 0$, is minimised at $\alpha^\star = E[me]/E[m^2]$, and satisfies $J(\alpha) < J(0)$ if and only if $\alpha \in (0,\ 2\alpha^\star)$, provided $E[me] > 0$:

$$J(\alpha) = E[e^2] - 2\alpha E[me] + \alpha^2 E[m^2], \qquad \alpha^\star = \frac{E[me]}{E[m^2]}. \tag{14}$$

Proof. Expanding J and differentiating gives $J'(\alpha) = -2E[me] + 2\alpha E[m^2]$, whence $\alpha^\star$.

Furthermore $J(\alpha) - J(0) = \alpha(\alpha E[m^2] - 2E[me])$, which is negative exactly on the open interval between 0 and $2E[me]/E[m^2] = 2\alpha^\star$. □

Corollary 1 (optimal attainable improvement). At $\alpha = \alpha^\star$, $J(\alpha^\star) = (1 - \rho_0^2)E[e^2]$, where $\rho_0 = E[me]/\sqrt{E[m^2]E[e^2]}$. Here ρ_0 is an uncentred alignment coefficient (cosine similarity), not the usual mean-centred Pearson correlation. The optimal attainable RMSE reduction is $1 - \sqrt{1 - \rho_0^2}$:

$$J(\alpha^\star) = (1 - \rho_0^2)E[e^2], \qquad \rho_0 = \frac{E[me]}{\sqrt{E[m^2]E[e^2]}}, \qquad 1 - \sqrt{1 - \rho_0^2}. \tag{15}$$

Corollary 1 provides an ex ante estimate only when ρ_0 is measured on a representative training or validation distribution and transfers to deployment. Test-set ρ_0 is reported here as a retrospective diagnostic of that transfer, not as information available before evaluation.

The exact condition of Proposition 1 cannot be checked online because e_k is unobservable. The following trust region and innovation gate are therefore observable surrogates intended to limit harmful corrections; they do not logically enforce the oracle sign-and-magnitude condition:

$$\mathcal{T}_k = \left\{\Delta \in \mathbb{R}:\ |\Delta| \le \kappa\sqrt{P_k^{SOC}}\right\}, \qquad \kappa > 0. \tag{16}$$

Second, an innovation gate admits a correction only when the linearised a posteriori measurement residual does not exceed a tolerance multiple of its uncorrected value:

$$g_k = \mathbb{1}\{|y_k - h(\hat{\mathbf{x}}_{k|k} + \Delta\mathbf{e}_1, u_k)| \le \gamma|y_k - h(\hat{\mathbf{x}}_{k|k}, u_k)|\}, \qquad \gamma \ge 1. \tag{17}$$

The tolerance γ controls the gate: $\gamma = 1$ is strict, while $\gamma \to \infty$ disables it. Because measurement-residual direction need not equal state-error direction, even $\gamma = 1$ is a risk heuristic rather than a pointwise non-degradation certificate. κ and γ are selected on the validation partition only.

With e_1 the first canonical basis vector. The applied correction is therefore:

$$\Delta_k = g_k\,\Pi_{\mathcal{T}_k}(\hat{\alpha}\,m_k), \qquad \Pi_{\mathcal{T}_k}(\xi) = \mathrm{sgn}(\xi)\min\left(|\xi|,\ \kappa\sqrt{P_k^{SOC}}\right), \tag{18}$$

where $\hat{\alpha}$ is the shrinkage gain estimated on the validation set by (Proposition 2) least squares. The operator Π is the Euclidean projection onto the trust region and is therefore non-expansive; g_k is a hard gate that reverts the estimator exactly to its baseline whenever the correction fails the residual test.

Lemma 1 (conditional mean-square boundedness). Suppose the baseline error satisfies $E[e_k^2] \le \bar{\sigma}^2$ and the posterior SOC variance satisfies $E[P_k^{SOC}] \le c\,E[e_k^2]$ for some finite c. Then any correction projected by Eq. (18) satisfies $E[\tilde{e}_k^2] \le \left(1 + \kappa\sqrt{c}\right)^2\bar{\sigma}^2$. If the oracle condition of Proposition 1 also holds at every step, then $E[\tilde{e}_k^2] \le \bar{\sigma}^2$:

$$E[\tilde{e}_k^2] \le \left(1 + \kappa\sqrt{c}\right)^2\bar{\sigma}^2. \tag{19}$$

Proof. Projection gives $E[\Delta_k^2] \le \kappa^2 E\left[P_k^{\mathrm{SOC}}\right] \le \kappa^2 c\,E[e_k^2]$. Minkowski's inequality yields $\|\tilde{e}_k\|_2 \le \|e_k\|_2 + \|\Delta_k\|_2 \le \left(1 + \kappa\sqrt{c}\right)\|e_k\|_2$, which proves the first bound. The second follows directly from Proposition 1. □

3.5. Health indices for the SOH stage

All indices are computed from estimated quantities only. Let W denote a sliding window of length N_W.

Resistance health index – decreasing in resistance growth relative to nominal:

$$\rho_R(t) = \exp\left(-\gamma_R \max\left\{0,\ \frac{\hat{R}_{0,nom}(t)}{R_{0,0}} - 1\right\}\right), \qquad \hat{R}_{0,nom} = \frac{\hat{R}_0}{1 + \alpha\left(\bar{T} - T_{ref}\right)}. \tag{20}$$

Thermal-memory health index – exponentially weighted accumulated temperature excess at the monthly-session scale:

$$H_{\theta,m} = 0.75\, H_{\theta,m-1} + 0.25\, \frac{\overline{\max\left(0,\ T - T_{ref}\right)}}{T_{scale}}, \qquad \rho_{\theta,m} = \exp\left(-H_{\theta,m}\right). \tag{21}$$

Excitation-quality index – informativeness of the recent current profile for parameter identification, normalised to unity at or above the reference excitation level:

$$\rho_I(t) = \min\left\{1,\ \frac{std_W(I)}{I_{ref}}\right\}. \tag{22}$$

Electrochemical-consistency index – agreement between measured and model-expected terminal voltage:

$$\rho_V(t) = \exp\left(-\frac{1}{\sigma_v}\sqrt{\frac{1}{N_W}\sum_{j \in W}\left(y_j - \hat{y}_j\right)^2}\right). \tag{23}$$

Each index lies in (0, 1], equals unity for a cell operating at nominal condition under informative excitation, and decreases with the corresponding stress or inconsistency. With this orientation, "thermal HIGH" unambiguously denotes low accumulated thermal stress. The learned 32-rule grid is described in Section 3.6.

The fixed index parameters are $\gamma_R = 1.6$, thermal-memory factor 0.75, $T_{scale} = 12$ °C, $I_{ref} = 8$ A, $\sigma_v = 3.0$ mV and $N_W = 480$ samples (one 8 h session at 60 s sampling). These scaling values were set before test evaluation to map the simulated operating envelope to numerically useful health scores; they were not fitted to test labels.

3.6. SOH inference module

The SOH stage is a second first-order Sugeno ANFIS with five inputs: the four health indices and the monthly mean corrected SOC. It predicts the residual of the UKF-derived SOH proxy from Eq. (7). Because no posterior SOH covariance is available, the SOC trust-region operator is not reused; the applied SOH correction is clipped to ±0.24, a validation-fixed numerical bound:

$$SOH_m^{hyb} = SOH_m^{UKF} + clip\left[\hat{\alpha}_{SOH}\, G\left(\rho_R, \rho_\theta, \rho_I, \rho_V, \overline{SOC^{hyb}}\right),\ -0.24,\ 0.24\right]. \tag{24}$$

G uses two generalised-bell membership functions per input, producing all $2^5 = 32$ grid-partition rules. The rules and first-order consequent coefficients are learned; there is no separate hand-coded nine-rule base. Table 4 states the complete reproducible configuration.

Table 4. Reproducible configuration of the SOH inference module

Item	Setting	Implementation note	Leakage control
Inputs	ρ_R, ρ_θ, ρ_I, ρ_V, mean corrected SOC	5 inputs at monthly scale	Estimated quantities only
Membership functions	2 gbell functions per input	32 grid-partition rules	Initialised from training quantiles
Consequents	First-order Sugeno	Learned by regularised LSE	Training labels only
Epochs / stopping	60 max; patience 8	Validation early stopping	No test tuning
Training observations	18 runs × 24 sessions	Session-level labels	Models frozen before test
Correction bound	±0.24 SOH	Fixed clipping; not covariance-based	Selected without test labels

4. Experimental design

4.1. Data generation and structural model mismatch

Sensor noise and bias were applied independently to current, voltage and temperature channels. Reference trajectories were generated by a dual-polarisation 2RC circuit with hysteresis, temperature-dependent diffusion and a Peukert capacity correction, whereas all Kalman estimators used the 1RC model of Section 2.3. For the first test trajectory, the RMS generator-estimator voltage discrepancy under identical inputs and true SOC was 1.44 mV; after removing the best-fitting current-proportional component absorbable by $\hat{R}_0$ it was 0.50 mV. Thus the evaluation includes structural, not only parametric, mismatch.

Each eight-hour diagnostic session represents stationary standby service: low float current, simulated mains-outage discharge events, subsequent recharge and one capacity-verification discharge consistent with the test context of IEC 60896-21 [28]. Seven distinct profiles (A-G) vary event count, C-rate, duration, ripple and verification depth; their mean temperature bands span 12-31 °C. These are synthetic standard-context scenarios, not measurements from a railway site. Accordingly, the paper makes no claim of railway-specific validation.

4.2. Training, validation and test protocol

The Monte Carlo ensemble is partitioned at the level of complete trajectories, not of samples, and the partition is disjoint in the generating conditions and not merely in the noise seed:

Training set: runs spanning three distinct load profiles and three temperature bands. Training on a single profile was found to produce a corrector that did not transfer (Section 5.5), and profile diversity in training is treated here as a requirement rather than a refinement.

Validation set: runs under a fourth profile and temperature band, used only for early stopping, for estimating the shrinkage gain $\hat{\alpha}$, and for calibrating the trust-region radius κ and the gate tolerance γ.

Test set: runs generated under load profiles, temperature bands and ageing states not represented in training or validation.

The ANFIS modules and the normalisation statistics are fitted once on the training set and frozen; no model is retrained within any evaluation run, and no reference SOC or SOH value from any evaluation run is used at any point in fitting. Monte Carlo perturbation of a single trajectory is not by itself evidence of generalisation, and is not treated as such here: generalisation is claimed only across the independent load, temperature and ageing profiles of the test set.

The training partition comprised 18 runs: six each under A/A, F/F and G/G (load/temperature labels). The validation partition comprised six B/B runs. The test partition comprised 24 runs: eight each under C/C, D/D and E/E. Random seeds were disjoint across partitions. No reference SOC or SOH value, sample, trajectory, normalisation statistic or early-stopping decision from the test partition entered training or validation.

4.3. Baselines

Eleven estimators are compared. Five are model-based methods: EKF, UKF, adaptive UKF with Sage-Husa noise adaptation [30], a bootstrap particle filter [31], and a dual EKF with fast [SOC, V_p] and slow $[R_0, Q]$ filters. Two are standalone data-driven models: matched-capacity ANFIS (Table 3) and gradient-boosted regression. A published-hybrid baseline implements the Kalman-filter-first EKF-ANN architecture described by Dao et al. [32], using $[I, T, V, SOC^{EKF}]$ as inputs to a 32-16 neuron tanh MLP trained on 60 000 training samples with early stopping. This is a protocol-matched adaptation to VRLA data, not a claim of reproducing the original Li-ion numerical result. Two simpler residual-correction ablations use the same UKF and online risk controls:

Proportional correction: $\Delta_k = \alpha \bar{v}_k$, a single scalar gain on the normalised innovation.

Linear correction: $\Delta_k = \theta^T \varphi_k$ with $\varphi_k = [1, I_k, \Delta I_k, T_k, \bar{v}_k]^T$, fitted by least squares on the same training set.

The eleventh method is the proposed ANFIS correction. The proportional and linear ablations isolate the value of nonlinear neuro-fuzzy representation, while the published EKF–ANN baseline provides the previously missing comparison with an existing Kalman-filter/data-driven hybrid architecture.

4.4. Error metrics and normalisation

Five error metrics are computed for each run and estimator: RMSE, MAE, MaxAE, mean signed error (bias) and error standard deviation. These metrics are complementary but not statistically independent – $RMSE^2 = bias^2 + StdError^2$ identically, and MAE and MaxAE derive from the same error sequence – and a first-place ranking under all five is therefore descriptive evidence of a broad-based advantage, not five independent confirmations. The text and conclusions are worded accordingly.

For the normalised multi-criteria profile, each metric is mapped so that unity denotes the best estimator, using the absolute value for the signed bias:

$$s_a^{(m)} = \frac{\min_b \left|\mu_b^{(m)}\right|}{\left|\mu_a^{(m)}\right|}, \tag{25}$$

where $\mu_a^{(m)}$ is the ensemble mean of metric m for estimator a. Minimisation of |bias| rather than of the signed bias is stated explicitly because the two differ whenever any estimator exhibits negative bias, as several do here.

4.5. Statistical analysis

Each Monte Carlo run constitutes a block within which every estimator is evaluated under identical conditions. The primary analysis is the Friedman rank test across estimators within blocks [33], with Kendall's W as effect size. Post-hoc comparisons use paired Wilcoxon signed-rank tests with Holm-Bonferroni correction [34]. For each comparison we report the mean paired difference, its bias-corrected and accelerated bootstrap 95 % confidence interval and matched-pairs Cohen's d_z. No independent-sample ANOVA, unpaired t-test or uncomputed repeated-measures ANOVA is reported.

We describe the protocol as repeated Monte Carlo validation and make no claim that it is statistically powered, since no a priori effect-size assumption or sample-size calculation was performed. In place of such a claim we report the achieved precision: the half-width of the 95 % confidence interval on each mean paired difference.

The study uses 24 independent test runs as blocks. The achieved precision is reported through

the half-width of each bootstrap confidence interval in Table 8; no a priori power claim is made.

5. Results

Each run contained 24 monthly diagnostic sessions of 8 h sampled every 60 s. There were 18 training, 6 validation and 24 independent test runs. Mean reference SOH declined monotonically from 99.3 % to 76.6 %; end-of-horizon values ranged from 69.0 to 87.2 % across test profiles.

5.1. Baseline filter behaviour and calibration

The normalised innovation of the baseline UKF had standard deviation 1.07, close to the nominal value of one. This is a measurement-residual diagnostic and is not presented as proof of the covariance condition assumed in Lemma 1. Measurement-noise standard deviation was 2.0 mV, and the structural voltage mismatch was 1.44 mV RMS (0.50 mV after removing the current-proportional component).

The UKF did not outperform the EKF on these data: SOC RMSE was 1.314 % against 1.192 %. Over the operating envelope reached here the OCV–SOC characteristic is close to affine across most of the traversed range, so the linearisation error that sigma-point propagation avoids is small, while the additional sigma-point spread increased the variance of the estimate. We therefore treat the selection of the UKF as the baseline as a design decision and not as an empirically established superiority.

Validation-only calibration selected $\kappa = 8$ and $\gamma = 10^9$ (effectively an inactive innovation gate). On the test partition projection was active for 0.76 % of samples and the gate rejected none. Thus the accuracy-selected configuration does not empirically demonstrate pointwise non-degradation. In a deliberately adversarial sign-reversed-correction test, ungated RMSE rose from the UKF's 1.314 % to 2.241 %. Strict controls ($\kappa = 2$, $\gamma = 1$) rejected 64.3 % of corrections and limited RMSE to 1.386 %, but did not preserve the baseline value. This result supports the narrower claim that the controls limit risk; it also falsifies any stronger claim that they enforce Proposition 1 without access to the true state error.

5.2. SOC estimation accuracy

The proposed estimator attained the lowest RMSE (0.942 %), MAE (0.484 %) and error standard deviation (0.940 %). It reduced RMSE by 28.3 % relative to its UKF baseline and by 7.8 % relative to the linear-correction ablation. The protocol-matched published EKF-ANN baseline obtained 1.675 %. The proposed method did not rank first on MaxAE or absolute bias; those outcomes remain visible in Table 5 and Fig. 5.

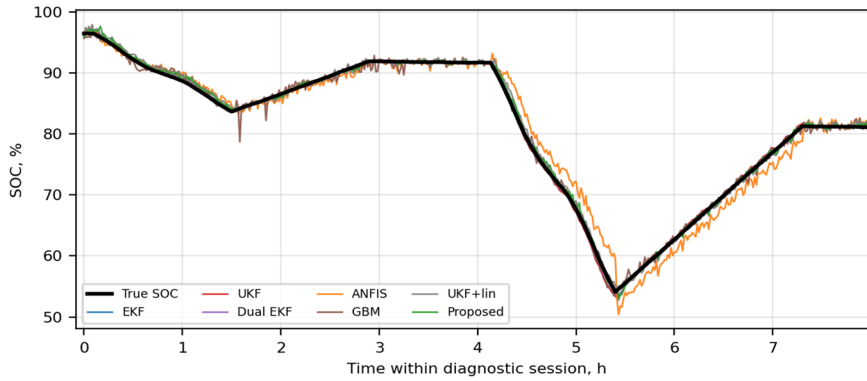

Fig. 2. Representative SOC estimation trajectories within one diagnostic session, under a deliberately biased initial condition

ISSN PRINT 2351-5279, ISSN ONLINE 2424-4627

The standalone ANFIS had the smallest MaxAE (9.537 %), while the linear corrector had the smallest absolute bias (0.006 %). Accordingly, a first-place result for RMSE is not described as universal superiority across error criteria.

Table 5. SOC estimation errors over 24 independent test runs (%, mean ± s.d. for RMSE; ensemble means for other metrics)

Estimator	RMSE	MAE	MaxAE	Bias	StdError
EKF	1.192 ± 0.126	0.673	17.247	−0.253	1.165
UKF	1.314 ± 0.442	0.708	18.138	−0.257	1.286
Adaptive UKF	2.232 ± 0.633	1.190	17.443	−0.603	2.136
Particle filter	4.523 ± 1.563	2.894	22.955	−0.981	4.414
Dual EKF	1.558 ± 0.430	0.842	17.647	−0.255	1.536
ANFIS (standalone)	1.526 ± 0.278	1.050	9.537	+0.149	1.515
Gradient boosting	1.817 ± 0.683	1.210	13.575	+0.230	1.738
Published EKF–ANN [32]	1.675 ± 0.372	1.159	11.698	−0.478	1.586
UKF + proportional corr.	1.185 ± 0.463	0.731	14.637	−0.226	1.162
UKF + linear corr.	1.022 ± 0.432	0.597	14.491	−0.006	1.019
Proposed (UKF + ANFIS, TR)	0.942 ± 0.459	0.484	14.659	−0.031	0.940

5.3. Convergence behaviour

Two observations follow. The proposed estimator did not converge fastest: the particle filter, the dual EKF and both plain Kalman filters entered the tolerance band sooner, and the residual correctors were slower than their own baselines. Any claim that residual correction improves transient responsiveness is therefore unsupported by these data and is not made. Second, because steady-state RMSE is of the same order as the 1 % tolerance band, this diagnostic is sensitive to small threshold crossings. It is retained only to expose the slower transient as a genuine cost of the correction.

Table 6. Time until absolute SOC error entered and remained within a 1 % band during the first diagnostic session

Estimator	Mean, h	s.d., h
EKF	5.878	1.958
UKF	5.944	1.976
Adaptive UKF	6.673	1.356
Particle filter	5.386	2.170
Dual EKF	5.826	2.327
ANFIS (standalone)	7.925	0.052
Gradient boosting	7.811	0.167
Published EKF–ANN [32]	7.767	0.267
UKF + proportional corr.	7.276	0.946
UKF + linear corr.	7.685	0.245
Proposed (UKF + ANFIS, TR)	6.671	0.770

5.4. SOH estimation accuracy

The SOH result is negative for the neuro-fuzzy stage. The UKF-derived proxy had 12.292 % RMSE; ANFIS correction reduced it to 5.167 %, but the linear corrector reached 1.449 % and the standalone ANFIS 2.678 %. This demonstrates that the indices contain useful information but that the 32-rule residual ANFIS overfits the limited session-level training set.

5.5. Ablation: what does the neuro-fuzzy structure contribute?

Against the same UKF residual and online controls, proportional correction achieved 1.185 % RMSE and linear correction 1.022 %, versus 0.942 % for ANFIS. The paired linear-versus-ANFIS

difference was 0.080 percentage points (95 % BCa CI [0.062, 0.094], $d_z = 2.03$, Holm-adjusted $p = 2.1\times10^{-6}$). Most of the benefit therefore comes from residual correction itself; ANFIS adds a smaller but reliable increment under these conditions.

This decomposition is consistent with Corollary 1: additional model capacity matters only insofar as it improves transferable alignment with the baseline error. The simpler linear corrector is preferable unless the 0.080-point improvement justifies the added complexity.

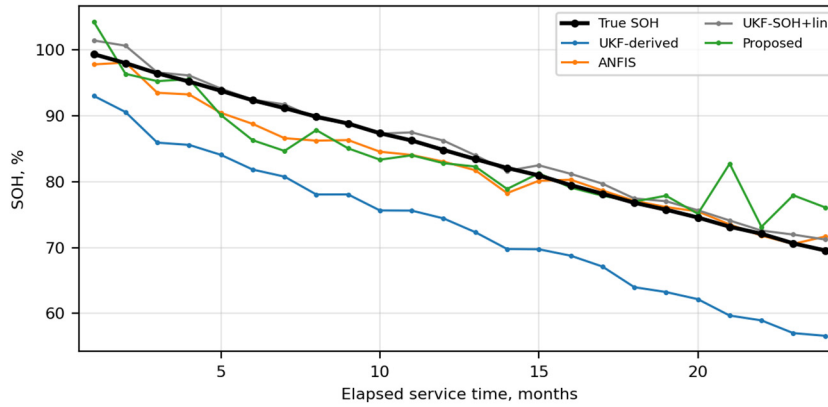

Fig. 3. SOH estimation over the 24-month ageing horizon. The reference trajectory declines monotonically, as required of a cumulative degradation quantity

Table 7. SOH estimation errors over the 24-month ageing trajectory (%, mean ± s.d. for RMSE; ensemble means for other metrics)

Estimator	RMSE	MAE	MaxAE	Bias	StdError
UKF-derived SOH (Eq. (7))	12.292±0.713	12.169	14.715	−12.169	1.623
ANFIS (standalone)	2.678±1.510	2.157	5.877	+0.533	1.880
UKF-SOH + linear corr.	1.449±0.620	1.135	3.680	+0.120	1.130
Proposed SOH correction	5.167±1.348	3.857	13.169	−0.750	4.394

5.6. Consistency with the theoretical prediction

The uncentred alignment coefficient was $\rho_0 = 0.696$ on training and 0.716 on the independent test partition; the shrinkage gain $\hat{\alpha} = 0.953$ was estimated from validation data. Test alignment corresponds to an optimal attainable RMSE reduction of 30.2 %, whereas the validation-scaled correction achieved 28.3 %. This close agreement is a retrospective transfer diagnostic, not a test-informed prediction.

The training value alone implies an optimal reduction of 28.2 %, essentially the 28.3 % observed. Similar training and test alignment indicates that the correction signal transferred across the deliberately disjoint profile sets. A reduction far above that implied by pre-test alignment would instead be a warning to audit the pipeline for leakage.

An earlier configuration of this study, in which the corrector was trained on a single load profile, gave $\hat{\rho} = 0.842$ on training against a measured reduction of 5.7 % – a gross discrepancy in the opposite direction. Corollary 1 diagnosed that failure correctly as a collapse of ρ on unseen conditions, and the remedy, training across three profiles, was identified from the discrepancy alone without access to the test partition. We report this because it demonstrates the diagnostic in the role for which it is intended.

For SOH, training alignment was 0.997 but test accuracy was poor. With 32 rules fitted to session-level observations, this is a clear over-parameterisation signature; the 1.449 % linear-correction RMSE confirms that the input indices, rather than the availability of predictive information, are not the main limitation.

5.7. Statistical analysis and multi-criteria ranking

The randomised-block analysis used 24 test runs. Across eleven SOC estimators, the Friedman test gave $\chi^2(10) = 172.3$, $p = 9.4\times10^{-32}$ and Kendall's $W = 0.718$. Across four SOH estimators, $\chi^2(3) = 65.85$, $p = 3.3\times10^{-14}$ and $W = 0.915$. Holm-corrected paired Wilcoxon results, mean differences, BCa intervals and d_z are reported in Table 8.

Table 8. Paired comparisons of SOC RMSE against the proposed estimator, 24 test runs. A positive difference favours the proposed estimator

Comparison (SOC RMSE)	Mean paired Δ	95 % CI (BCa)	d_z	Holm-adj. p
EKF vs proposed	+0.250	[+0.012, +0.368]	+0.61	0.0025
UKF vs proposed	+0.372	[+0.333, +0.417]	+3.46	1.2×10^{-6}
Adaptive UKF vs proposed	+1.290	[+1.129, +1.643]	+2.20	1.2×10^{-6}
Particle filter vs proposed	+3.581	[+3.047, +4.153]	+2.51	1.2×10^{-6}
Dual EKF vs proposed	+0.616	[+0.452, +0.779]	+1.47	6.0×10^{-6}
ANFIS (standalone) vs proposed	+0.584	[+0.288, +0.747]	+1.06	7.5×10^{-4}
Gradient boosting vs proposed	+0.875	[+0.496, +1.185]	+1.01	4.5×10^{-4}
Published EKF–ANN [32] vs proposed	+0.733	[+0.481, +0.931]	+1.31	3.3×10^{-5}
UKF + proportional corr. vs proposed	+0.243	[+0.193, +0.301]	+1.76	1.2×10^{-6}
UKF + linear corr. vs proposed	+0.080	[+0.062, +0.094]	+2.03	2.1×10^{-6}

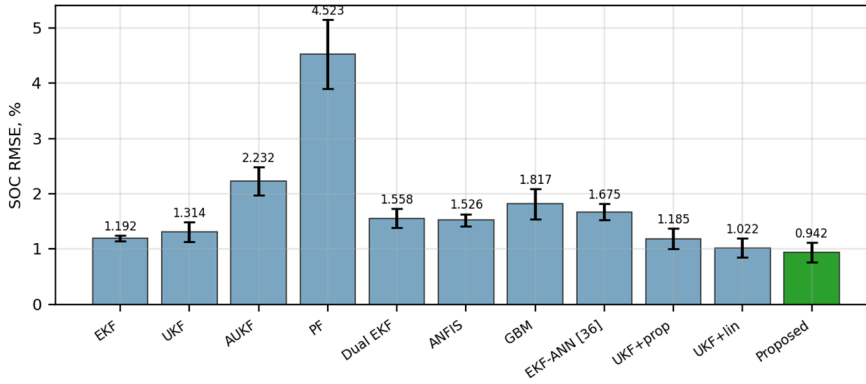

Fig. 4. Mean SOC RMSE with 95 % confidence intervals over 24 test runs

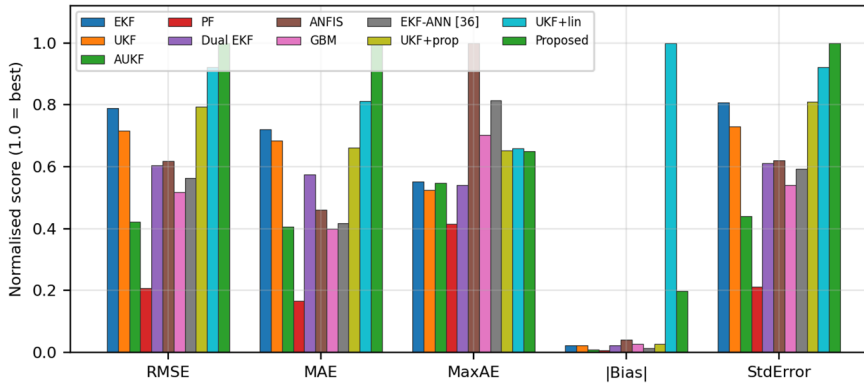

Fig. 5. Normalised multi-metric profile for SOC estimation, Eq. (25); unity denotes the best estimator on each metric and the signed bias is ranked by absolute value

For SOH, the ANFIS correction improved on the UKF-derived proxy by 7.125 percentage points (95 % CI [6.468, 7.556], $d_z = 5.32$), but was outperformed by standalone ANFIS by 2.489

points and by the linear corrector by 3.718 points; all Holm-adjusted $p = 3.6\times10^{-7}$.

The proposed SOC estimator attains the best normalised score for RMSE, MAE and error standard deviation, but not for MaxAE or absolute bias. The full profile is reported because the five metrics are derived from the same error sequences and are not independent confirmations.

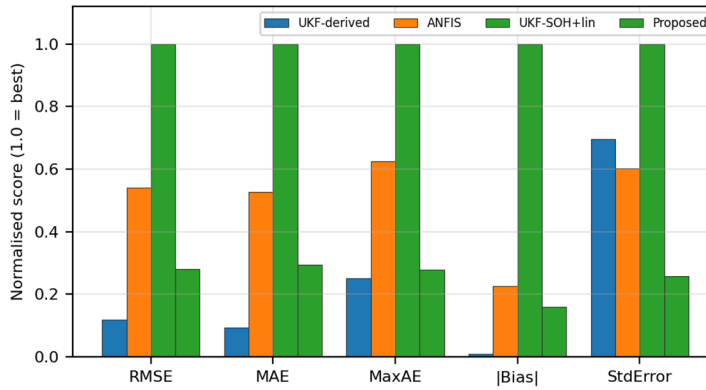

Fig. 6. Normalised multi-metric profile for SOH estimation, Eq. (25)

6. Discussion

The central mathematical result is the distinction between an exact oracle condition and implementable online surrogates. Proposition 1 identifies when an additive correction truly cannot degrade a scalar estimate. Proposition 2 and Corollary 1 quantify the optimal mean-square improvement through ρ_0. The covariance projection and innovation gate cannot verify the oracle sign condition; their contribution is boundedness and empirical risk limitation, as the adversarial test demonstrates.

Three practical consequences follow. First, pre-test alignment provides a compact criterion for deciding whether a corrector is promising. Second, model capacity must earn its cost through transferable alignment: the linear corrector captured most of the SOC gain. Third, protocol-matched comparison matters: the published EKF-ANN baseline [32] reached 1.675 % RMSE, while the proposed method reached 0.942 %, but this comparison is still simulation-based and chemistry-adapted.

Several findings qualify the method. UKF did not outperform EKF on this operating envelope. Residual correction improved overall RMSE but slowed entry into the 1 % band. The online risk controls were inactive at their accuracy-selected setting, and strict settings reduced but did not eliminate harm under a sign-reversed correction. Finally, the SOH ANFIS was inferior to a linear corrector. These negative results are retained because they define the method's actual scope.

Several limitations bound the interpretation of these findings.

(i) The exact pointwise condition depends on unobservable true error. The online projection and gate are risk-limiting surrogates, not a certificate; in the sign-reversal stress test they reduced RMSE damage from 2.241 % to 1.386 % but did not preserve the 1.314 % baseline.

(ii) The SOH corrector was over-parameterised for the number of session-level observations available, and its 32-rule structure should be reduced or replaced before the cascade is proposed for SOH use. That the linear corrector reached 1.44 % on the same inputs indicates that the health indices of Section 3.5 carry the necessary information and that the deficiency lies in the inference module alone.

(iii) Capacity is weakly observable within an 8 h diagnostic window, which is the proximate cause of the 12.17-point bias in the SOH baseline. A dual-estimation structure identifying capacity on the slow timescale, rather than within the fast filter, is the natural remedy and is likely to matter more than the choice of corrector.

(iv) The validation remains simulation-based. Although the generator is structurally distinct from the estimator, no physical measurement is involved, and the uncertainty contributed by physical capacity and resistance measurement, sensor calibration drift and ageing heterogeneity between cells is absent; the metrological treatment of calibration and uncertainty evaluation required for a field implementation is discussed for a comparable monitoring context in [35].

(v) The framework was parameterised for a single cell type from a single manufacturer, and the ageing model of Section 2.4, while calibrated to a physically plausible 24-month decline, was not fitted to measured ageing data for this cell.

(vi) The duty profiles are synthetic stationary-standby scenarios informed by IEC 60896-21, not recordings from an operating railway installation. Railway systems are therefore an intended application only.

(vii) Lemma 1 gives a boundedness result conditional on the baseline satisfying the error bound of [36] and on a relation between posterior covariance and true error. That relation is not proved or empirically verified here; the reported normalised innovation is only a measurement-residual diagnostic.

7. Conclusions

This paper establishes exact pointwise and mean-square conditions for beneficial additive residual correction. The result shows why the fact that a zero correction reproduces the baseline is not a guarantee for a learned non-zero correction. It also expresses the optimal attainable mean-square error as $(1-\rho_0^2)$ times the baseline error. Observable trust-region projection and innovation gating provide conditional boundedness and empirical risk limitation, but not oracle pointwise non-degradation.

For a Sonnenschein A602/280 VRLA gel cell under structural model mismatch, online parameter estimation, a 24-month ageing horizon and disjoint profile-level data partitions, the proposed SOC estimator reduced RMSE from 1.314 % to 0.942 %. It was best among eleven tested estimators, including the protocol-matched published EKF-ANN architecture (1.675 %), although the linear residual corrector was close at 1.022 %. Training alignment implied a 28.2 % optimal reduction and the observed reduction was 28.3 %. The SOH ANFIS stage was inferior to the linear corrector.

The practical conclusion is that residual correction should be justified by transferable alignment and compared against simple correctors, while online gates should be evaluated under deliberately failed learned models rather than described as guarantees. Future work requires experimental VRLA ageing data, a slow-timescale capacity estimator and a reduced SOH model.

Acknowledgements

The authors have not disclosed any funding.

The authors express their gratitude to the Electrical Engineering Department of Tashkent State Transport University for providing the computational resources and academic environment that supported this research.

Data availability

The datasets generated during and/or analyzed during the current study are available from the corresponding author on reasonable request.

Author contributions

Otabek Boltaev: validation, resources, writing-review and editing. Igor Kolesnikov: conceptualization, methodology, formal analysis, resources, writing-review and editing, supervision. Karimberdi Karshiev: conceptualization, methodology, software, formal analysis,

validation, investigation, writing-original draft, writing-review and editing, visualization.

Conflict of interest

The authors declare that they have no conflict of interest.

References

[1] "Global EV outlook 2025," International Energy Agency, Paris, France, 2025.

[2] M. Berecibar, I. Gandiaga, I. Villarreal, N. Omar, J. van Mierlo, and P. van den Bossche, "Critical review of state of health estimation methods of Li-ion batteries for real applications," *Renewable and Sustainable Energy Reviews*, Vol. 56, pp. 572–587, Dec. 2015, https://doi.org/10.1016/j.rser.2015.11.042

[3] R. Aliev, M. Aliev, and G. Talipova, "Mathematical model and algorithm for determining the shunt zone by train," in *AIP Conference Proceedings*, Vol. 3447, No. 1, p. 020004, May 2026, https://doi.org/10.1063/12.0044000

[4] M. Yakubov, M. Talipov, and U. Nurullaev, "An optimized Lagrangian approach to reactive power compensation in nonlinear traction power-supply systems," *Vibroengineering Procedia*, Vol. 60, pp. 724–730, Dec. 2025, https://doi.org/10.21595/vp.2025.25604

[5] Z. Bagova et al., "Processing of lead-containing industrial waste in Kazakhstan," *Open Engineering*, Vol. 16, No. 1, p. 20250156, Jan. 2026, https://doi.org/10.1515/eng-2025-0156

[6] W. Waag, C. Fleischer, and D. U. Sauer, "Critical review of the methods for monitoring of lithium-ion batteries in electric and hybrid vehicles," *Journal of Power Sources*, Vol. 258, pp. 321–339, Mar. 2014, https://doi.org/10.1016/j.jpowsour.2014.02.064

[7] H. He, R. Xiong, and J. Fan, "Evaluation of lithium-ion battery equivalent circuit models for state of charge estimation by an experimental approach," *Energies*, Vol. 4, No. 4, pp. 582–598, Mar. 2011, https://doi.org/10.3390/en4040582

[8] M. Simic, A. K. Stavrakis, V. Jeoti, and G. M. Stojanovic, "A Randles circuit parameter estimation of Li-ion batteries with embedded hardware," *IEEE Transactions on Instrumentation and Measurement*, Vol. 71, pp. 1–12, Jun. 2022, https://doi.org/10.1109/tim.2022.3183661

[9] J. Estaller, A. Kersten, M. Kuder, T. Thiringer, R. Eckerle, and T. Weyh, "Overview of battery impedance modeling including detailed state-of-the-art cylindrical 18650 lithium-ion battery cell comparisons," *Energies*, Vol. 15, No. 10, p. 3822, May 2022, https://doi.org/10.3390/en15103822

[10] G. L. Plett, "Extended Kalman filtering for battery management systems of LiPB-based HEV battery packs: Part 2. Modeling and identification," *Journal of Power Sources*, Vol. 134, No. 2, pp. 262–276, 2004, https://doi.org/10.1016/j.jpowsour.2004.02.032

[11] R. E. Kalman, "A new approach to linear filtering and prediction problems," *Journal of Basic Engineering*, Vol. 82, No. 1, pp. 35–45, Mar. 1960, https://doi.org/10.1115/1.3662552

[12] S. J. Julier and J. K. Uhlmann, "Unscented filtering and nonlinear estimation," *Proceedings of the IEEE*, Vol. 92, No. 3, pp. 401–422, Mar. 2004, https://doi.org/10.1109/jproc.2003.823141

[13] H. He, H. Qin, X. Sun, and Y. Shui, "Comparison study on the battery SoC estimation with EKF and UKF algorithms," *Energies*, Vol. 6, No. 10, pp. 5088–5100, Sep. 2013, https://doi.org/10.3390/en6105088

[14] A. Khalid et al., "Comparison of Kalman filters for state estimation based on computational complexity of Li-ion cells," *Energies*, Vol. 16, No. 6, p. 2710, Mar. 2023, https://doi.org/10.3390/en16062710

[15] J.-S. R. Jang, "ANFIS: adaptive-network-based fuzzy inference system," *IEEE Transactions on Systems, Man, and Cybernetics*, Vol. 23, No. 3, pp. 665–685, Aug. 2002, https://doi.org/10.1109/21.256541

[16] C. H. Cai, D. Du, and Z. Y. Liu, "Battery state-of-charge (SOC) estimation using adaptive neuro-fuzzy inference system (ANFIS)," in *The 12th IEEE International Conference on Fuzzy Systems, 2003. FUZZ '03*, Vol. 2, pp. 1068–1073, 2004, https://doi.org/10.1109/fuzz.2003.1206580

[17] Z. Cui, J. Dai, J. Sun, D. Li, L. Wang, and K. Wang, "Hybrid methods using neural network and Kalman filter for the state of charge estimation of lithium-ion battery," *Mathematical Problems in Engineering*, Vol. 2022, pp. 1–11, May 2022, https://doi.org/10.1155/2022/9616124

[18] P. Ruetschi, "Aging mechanisms and service life of lead-acid batteries," *Journal of Power Sources*, Vol. 127, No. 1-2, pp. 33–44, Dec. 2003, https://doi.org/10.1016/j.jpowsour.2003.09.052

[19] H. A. Catherino, F. F. Feres, and F. Trinidad, "Sulfation in lead-acid batteries," *Journal of Power Sources*, Vol. 129, No. 1, pp. 113–120, Feb. 2004, https://doi.org/10.1016/j.jpowsour.2003.11.003

[20] K. Nakamura, M. Shiomi, K. Takahashi, and M. Tsubota, "Failure modes of valve-regulated lead/acid batteries," *Journal of Power Sources*, Vol. 59, No. 1-2, pp. 153–157, Jul. 2002, https://doi.org/10.1016/0378-7753(95)02317-8

[21] L. T. Lam, N. P. Haigh, C. G. Phyland, and A. J. Urban, "Failure mode of valve-regulated lead-acid batteries under high-rate partial-state-of-charge operation," *Journal of Power Sources*, Vol. 133, No. 1, pp. 126–134, Jan. 2004, https://doi.org/10.1016/j.jpowsour.2003.11.048

[22] J. Schiffer, D. U. Sauer, H. Bindner, T. Cronin, P. Lundsager, and R. Kaiser, "Model prediction for ranking lead-acid batteries according to expected lifetime in renewable energy systems and autonomous power-supply systems," *Journal of Power Sources*, Vol. 168, No. 1, pp. 66–78, Dec. 2006, https://doi.org/10.1016/j.jpowsour.2006.11.092

[23] Y. Li et al., "Data-driven health estimation and lifetime prediction of lithium-ion batteries: A review," *Renewable and Sustainable Energy Reviews*, Vol. 113, p. 109254, Jul. 2019, https://doi.org/10.1016/j.rser.2019.109254

[24] A. Farmann, W. Waag, A. Marongiu, and D. U. Sauer, "Critical review of on-board capacity estimation techniques for lithium-ion batteries in electric and hybrid electric vehicles," *Journal of Power Sources*, Vol. 281, pp. 114–130, Jan. 2015, https://doi.org/10.1016/j.jpowsour.2015.01.129

[25] R. Xiong, L. Li, and J. Tian, "Towards a smarter battery management system: A critical review on battery state of health monitoring methods," *Journal of Power Sources*, Vol. 405, pp. 18–29, Oct. 2018, https://doi.org/10.1016/j.jpowsour.2018.10.019

[26] M. Doshanova, M. Talipov, M. Shaazizova, N. Mirzayeva, S. Karaxanova, and I. Khodzamuratova, "Intelligent risk-oriented predictive diagnostics system based on vibration signal analysis," *Mathematical Models in Engineering*, Aug. 2026, https://doi.org/10.21595/mme.2026.26531

[27] "Sonnenschein A600 technical data: A602/225-A602/750." Exide Technologies, Technical data sheet. https://www.exidegroup.com/eu/en/document/sonnenschein-a600-datasheet

[28] *IEC 60896-21:2004, stationary lead-acid batteries – Part 21: Valve regulated types – methods of test*. Geneva: International Electrotechnical Commission, 2004.

[29] S. Santhanagopalan and R. E. White, "Online estimation of the state of charge of a lithium ion cell," *Journal of Power Sources*, Vol. 161, No. 2, pp. 1346–1355, Jun. 2006, https://doi.org/10.1016/j.jpowsour.2006.04.146

[30] A. P. Sage and G. W. Husa, "Adaptive filtering with unknown prior statistics," in *Joint Automatic Control Conference*, 1969.

[31] N. J. Gordon, D. J. Salmond, and A. F. M. Smith, "Novel approach to nonlinear/non-Gaussian Bayesian state estimation," *IEE Proceedings F Radar and Signal Processing*, Vol. 140, No. 2, p. 107, 2010, https://doi.org/10.1049/ip-f-2.1993.0015

[32] Q. Dao et al., "Design of an effective state of charge estimation method for a lithium-ion battery pack using extended Kalman filter and artificial neural network," *Energies*, Vol. 14, No. 9, p. 2634, May 2021, https://doi.org/10.3390/en14092634

[33] M. Friedman, "The use of ranks to avoid the assumption of normality implicit in the analysis of variance," *Journal of the American Statistical Association*, Vol. 32, No. 200, pp. 675–701, May 2012, https://doi.org/10.1080/01621459.1937.10503522

[34] S. Holm, "A simple sequentially rejective multiple test procedure," *Scandinavian Journal of Statistics*, Vol. 6, No. 2, pp. 65–70, 1979.

[35] A. Mamatov, X. Sotvoldiyev, M. Talipov, S. Shaumarov, K. Gafarbayli, and D. Bekmirzaev, "Metrological calibration and uncertainty evaluation of MEMS accelerometers for structural health monitoring in seismic regions," *Vibroengineering Procedia*, Vol. 62, pp. 140–144, Jun. 2026, https://doi.org/10.21595/vp.2026.26360

[36] K. Reif, S. Gunther, E. Yaz, and R. Unbehauen, "Stochastic stability of the discrete-time extended Kalman filter," *IEEE Transactions on Automatic Control*, Vol. 44, No. 4, pp. 714–728, Aug. 2002, https://doi.org/10.1109/9.754809



Otabek Boltayev holds the academic title of Professor at the Department of Electrical Engineering, Tashkent State Transport University, Tashkent, Uzbekistan. His current research interests include diagnostics and state estimation of stationary lead-acid and gel battery systems, and nonlinear Kalman filtering applications in energy-storage monitoring.



Igor Kolesnikov received the D.Sc. degree in Technical Sciences and holds the academic title of Professor at the Department of Electrical Engineering, Tashkent State Transport University, Tashkent, Uzbekistan. His current research interests include battery management systems, power estimation for energy-storage devices, and diagnostics of electrotechnical complexes.



Karimberdi Karshiyev is an independent researcher at the Department of Electrical Engineering, Tashkent State Transport University, Tashkent, Uzbekistan, currently pursuing a Ph.D. degree. His current research interests include state-of-charge and state-of-health estimation of lead-acid and lithium-ion batteries, Kalman filtering, and neuro-fuzzy inference systems.

ISSN PRINT 2351-5279, ISSN ONLINE 2424-4627